https://doi.org/10.5194/egusphere-2025-2434
Preprint. Discussion started: 23 June 2025

# Improving the relationship between soil texture and large-scale electromagnetic induction surveys using a direct current electrical resistivity calibration.

Joshua Thompson[1], Dimitrios Ntarlagiannis[1], Lee Slater[1,2]

[1]Department of Earth and Environmental Science, Rutgers University, Newark, 07102, United States
[2]Pacific Northwest National Laboratory, 902 Battelle Blvd, Richland, WA 99354 United States of America

*Correspondence to*: Joshua H. Thompson (jht51@rutgers.edu)

*Correspondence to* Dimitrios Ntarlagiannis (dimntar@newark.rutgers.edu)

*Correspondence to*: Lee Slater (lslater@newark.rutgers.edu)

https://doi.org/10.5194/egusphere-2025-2434
Preprint. Discussion started: 23 June 2025

## Abstract.

Ground-based electromagnetic induction (EMI) surveys can be used to infer soil properties and (by extension) support nutrient loss risk assessments of agricultural fields. The transport of nutrients from an agricultural field to surrounding surface waters depends on the hydrologic connectivity between the two systems, largely controlled by soil texture. Preexisting soil texture maps and associated soil drainage classifications are often used as proxy information to assess the potential for lateral migration of nutrients in the groundwater; however, the resolution of these maps is inadequate at the scale of individual fields. In this study, we evaluated whether the relationship between EMI data and soil texture was improved by calibrating the apparent electrical conductivity measured by an EMI sensor with a 2D electrical resistivity imaging (ERI) survey. The joint geophysical survey was performed across a ~1-ha field in Princess Anne, Maryland, United States. A calibration-inversion-comparison framework is presented that calibrates the EMI measurements using ERI conductivity models and subsequently inverts the EMI data. A robust validation scheme compared the calibrated and not calibrated EMI conductivity models against grain size, core-scale conductivity measurements and an ERI survey performed roughly 80 m from the first. This study shows that the calibration of EMI data with an ERI profile is significantly improves the quantitative relationship between EMI-derived electrical conductivity and representative soil properties, ensuring a finer-resolution proxy soil map for evaluating subsurface nutrient transport from agricultural fields.

## 1 Introduction

Precipitation-driven nutrient transport in agricultural landscapes is strongly controlled by soil texture that governs the hydrologic network to nearby surface waters (Heathwaite et al., 2000). Agricultural fields can promote surface runoff in fine-textured soils with low infiltration rates (Chardon & Schoumans, 2007; Lee et al., 2006; Needelman et al., 2004) and, in excess, can lead to soil erosion (Du et al., 2022). In low-relief and sloping landscapes, rapid subsurface nutrient transport occurs in groundwater flow (Kleinman, Peter JA et al., 2015; Vadas et al., 2007) through coarse-textured, even gravelly, soil inclusions (Fuchs et al., 2009; Gburek & Sharpley, 1998), and surface drainage tiles (Decker et al., 2024). Quite often, nutrient transport characterization of a field relies on regional look-up tables of soil hydraulic properties from the Soil Survey Geographic Database (SSURGO; Shober et al., 2017). While the SSURGO soil maps are still critical in evaluating nutrient loss from agricultural fields, most soil maps do not have a spatial resolution to account for within-field soil variability (Bjørn Møller et al., 2021; Krüger et al., 2013; Zhang & Feng, 2017). Two studies in the same low-relief, artificially-drained agricultural field exemplify the need for high-resolution spatial data to identify subsurface transport mechanisms. Robinson et al. (2020) observed relatively slow groundwater velocities during and after a natural rainfall event. In the same field, Thompson et al. (2025), just 80 m west, reported that a gravelly sand layer promoted rapid groundwater transport during a field-simulated rainfall event. Yet, the field is mapped as a single, poorly drained soil. These studies show that nutrient transport in groundwater occurs during transient hydrological events (e.g., rainfall or flooding), and the available pathways are determined by the textural properties of the soil below the resolution of the SSURGO soil maps.

Electromagnetic induction (EMI) and electrical resistivity imaging (ERI) are increasingly applied to map the variability in soil electrical conductivity (σ) across agricultural landscapes (Corwin & Scudiero, 2019; Triantafilis & Monteiro Santos, 2013). Among other soil properties, the σ is mostly influenced by soil water content, grain size, salinity, cation exchange capacity, and organic matter content (Friedman, 2005). Thus, field-scale EMI surveys have been used to infer landscape-wide variations in soil moisture (Martini et al., 2017; Sheets & Hendrickx, 1995), soil texture (Michael Mertens et al., 2008), depth-specific organic matter content (Huang et al., 2017), and groundwater salinization (Corwin & Plant, 2005; Lund et al., 1999). Relevant to nutrient transport, EMI surveys have provided qualitative predictions of hydrologically active regions of a 38-ha watershed (Abdu, H. et al., 2008). Brogi et al. (2019) used EMI data that predicted regions of plant stress across a 100-ha landscape validated against crop growth patterns from satellite images. While EMI surveys have provided insights into regional landscape characteristics, variations in moisture content and/or salinity can mask the dependence of σ on soil textural heterogeneity (Abdu, Hiruy et al., 2017).

Unlike the electrical resistivity geophysical method, EMI measurements only approximate σ. Compared to directly injecting current into the subsurface and measuring the voltage drop (i.e., ERI), the electromagnetic induction methods are more sensitive to environmental influences that can introduce noise into the measurements. EMI measurements can suffer from time-dependent drift due to atmospheric temperature changes (Minsley et al., 2014; Tan et al., 2019), tilting or rotating of the instrument on an uneven ground surface (Mclachlan et al., 2021), and cultural noise from power lines (Kiflai & Whitman, 2023). Therefore, EMI measurements are sometimes calibrated to reference data, such as direct soil core σ measurements (Moghadas et al., 2012) or field-scale σ measurements that improve the estimation of a true σ to invert for images more representative of the soil. Most relevant to our study, Lavoué et al. (2010) applied a linear regression-based calibration of EMI data with simulated EMI measurements from an inversion of an ERI dataset obtained on the same transect. Kiflai & Whitman (2023) used a similar approach to Lavoué et al. (2010) and used the calibrated EMI conductivity models to assess the spatial and temporal variability of a freshwater lens due to precipitation in the Florida Keys. Mclachlan et al. (2021) calibrated EMI measurements with co-located ERI conductivity models and found a strong relationship to the alluvial soil thickness in the Boxford Wetland, UK. The ERI calibration of EMI measurements tends to reduce the effect of noise on the EMI inversion, with the inversions producing more robust estimates of the subsurface conductivity structure (McLachlan et al., 2021; Mester et al., 2011; Minsley et al., 2014; von Hebel et al., 2014; Von Hebel et al., 2019). The impact of noise may be reduced by the ERI-informed calibration of EMI measurements; however, this method implicitly assumes the ERI inverted conductivity, used for the calibration of EMI data, perfectly represent subsurface features (Minsley et al., 2012). Both ERI and EMI inversion routines may over-smooth fine-scale features or overfit the data that may limit meaningful interpretations. Despite these limitations, the ERI-based calibration of EMI data prior to EMI inversion has improved the spatial correspondence of EMI images with borehole stratigraphy (Christiansen et al., 2016; Zaru et al., 2023) and lateral soil texture patterns (Von Hebel et al., 2014) relative to uncalibrated EMI inversions.

In this study, we show how ERI-informed calibration of EMI data improves the relationship between soil texture data and the inverted EMI conductivity model and propose a calibration-inversion-comparison (CIC) workflow to quantitatively evaluate the improvement. Conductivity models from the inversion of a co-located ERI dataset ($\sigma_{ERI}$[cal]) are used to simulate EMI measurements ($\sigma_{a,\ sim}$[cal]) via forward modeling. A series of calibration equations are then established between a subset of the raw EMI field measurements $\sigma_{a,\ EMI}$[nc] (nc refers to 'not calibrated' data) and $\sigma_{a,\ sim}$[cal] . The calibration equations are then applied to the entirety of the EMI measurements ($\sigma_{a,\ EMI}$[nc]) resulting in the calibrated apparent conductivity dataset $\sigma_{a,\ EMI}$[c]. The conductivity model obtained from the inversion of $\sigma_{a,\ EMI}$[c], defined here as $\sigma_{EMI}$[c], is validated against observational data not used in the calibration. Uncalibrated measurements $\sigma_{a,\ EMI}$[nc] are also inverted to obtain the uncalibrated EMI conductivity model $\sigma_{EMI}$[nc] and also compared against the same independent observational data. We demonstrate that, relative to $\sigma_{EMI}$[nc], $\sigma_{EMI}$[c] is strongly correlated with grain size, core-scale electrical conductivity measurements, and the inverted conductivity model ($\sigma_{ERI}$[val]) obtained from a second ERI profile located away from the calibration site. We also discuss the potential transferability of the calibration equations beyond a single field to six agricultural fields to facilitate a regional comparison of inverted EMI conductivity models.

## 3 Methods

### 3.1 The calibration-inversion-comparison (CIC) framework

Table 1 defines the variables that will be used in the three main steps of the CIC framework (Figure 1). Before the calibration, EMI measurements are simulated ($\sigma_{a,\ sim}$[cal]) for each coil configuration and instrument frequency based on $\sigma_{ERI}$[cal]. In the first stage (Fig. 3a), a linear regression is performed between $\sigma_{a,\ sim}$[cal] and $\sigma_{a,\ EMI}$[nc] to determine the regression model parameters. Subsequently, both $\sigma_{a,\ EMI}$[c] and $\sigma_{a,\ EMI}$[nc] are inverted using the same inversion settings (Fig. 3b) to produce the conductivity models $\sigma_{EMI}$[c] and $\sigma_{EMI}$[nc] respectively. These two EMI-derived conductivity models are compared against three datasets external to the calibration-inversion step (Fig 3d). The external datasets are soil grain size data, laboratory-scale measurements on soils cores, and the conductivity model $\sigma_{ERI}$[val] obtained for a second ERI profile performed away from the calibration profile. Comparisons between both $\sigma_{EMI}$[c] and $\sigma_{EMI}$[nc] and these external datasets were assessed using the Kling-Gupta Efficiency (KGE) measure, a common metric for model performance in hydrological modeling.

**Table 1.** Summary of the terminology used to refer to the different datasets and inverted models discussed in this paper.

| **Variable** | **Definition** |
|---|---|
| $\sigma_{a,\ EMI}[nc]$ | Not calibrated EMI measurements |
| $\sigma_{a,\ EMI}[c]$ | Calibrated EMI measurements |
| $\sigma_{EMI}[nc]$ | Inverted EMI measurements without calibration |
| $\sigma_{EMI}[c]$ | Inverted EMI measurements with calibration |
| $\sigma_{a,\ sim}[cal]$ | Simulated EMI apparent conductivity from inverted ERI conductivity for calibration |
| $\sigma_{a,\ sim}[inv]$ | Simulated EMI apparent conductivity from inverted EMI conductivity |
| $\sigma_{ERI}[cal]$ | Inverted ERI conductivity used to simulate $\sigma_{a,\ sim}[cal]$ |
| $\sigma_{ERI}[val]$ | Inverted from ERI conductivity used to validate $\sigma_{EMI}$[c] |

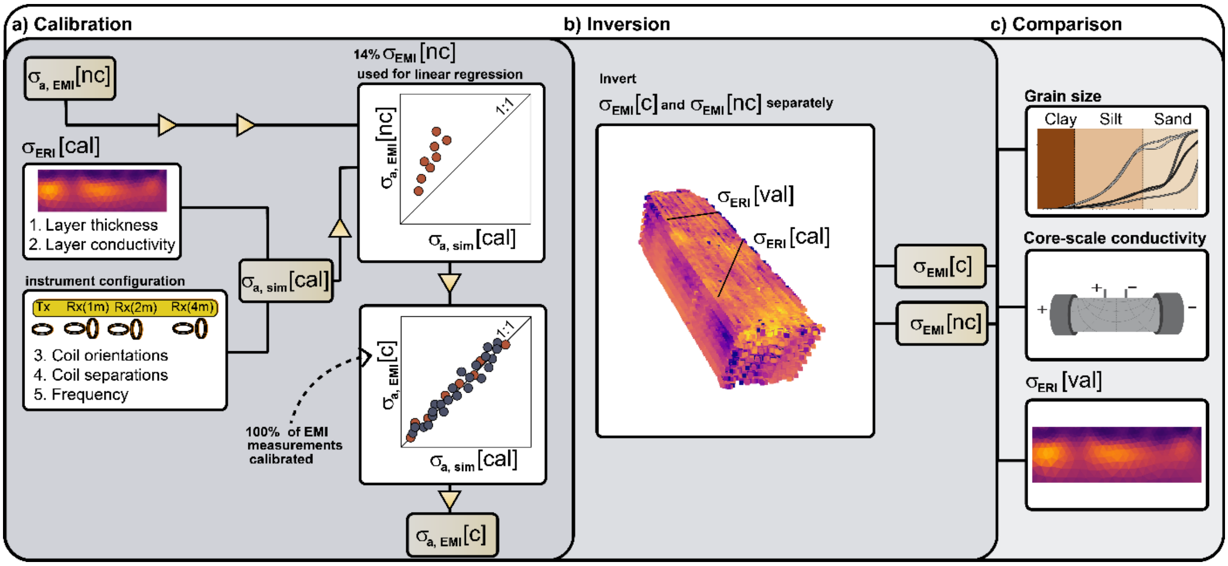

**Figure 1.** The calibration-inversion-comparison workflow. a) The first stage simulates apparent conductivity data using information from the $\sigma_{ERI}$ and the coil configurations of the EMI instrument. Then, in a) the entire EMI data set is calibrated with model parameters from the

linear regression between the simulated $\sigma_{a,\mathrm{EMI}}$, and the $\sigma_{\mathrm{EMI}}$[nc]. b) Invert both the calibrated and not calibrated EMI measurements. c) Determine if $\sigma_{\mathrm{EMI}}$[c] or $\sigma_{\mathrm{EMI}}$[nc] is more similar to data withheld from the calibration-inversion stages.

### 3.2 Site Description and Survey Layout

The 17000 $m^2$ agricultural field surveyed in this study is located on the Delmarva Peninsula, which lies on the eastern coast of the United States (Fig. 2a). The natural landscape of the lower Delmarva was primarily forest and marsh systems (Allen, 2009), including the farm, and necessitated drainage to lower the water tables and allow the land to be used for crop production. Artificial drainage likely facilitates an increase in the transport of subsurface nutrients. The geophysical surveys and direct soil sampling were performed between October 2019 and May 2022 at the University of Maryland Eastern Shore (UMES) research and teaching farm (referred to hereinafter as the farm) in Princess Anne, Maryland (MD; Fig. 2b). The fields at the farm are flat with a slope less than 2%; however, the study field contains localized regions of elevation change (<0.5 m) that likely influence runoff generation. The dominant soil series in the primary study field is defined as the Quindocqua series (fine-loamy, mixed, active, mesic Typic Endoaquults; (Soil Survey Staff, 2024) and mapped as Alisols (IUSS Working Group WRB, 2022). The north and south of the field contain the Manokin soil series (fine-loamy, mixed, active, mesic Aquic Hapludults) and are also mapped as Alisols (IUSS Working Group WRB, 2022). We conducted EMI surveys on seven additional agricultural fields on the Delmarva. Five of these fields predominantly contain a soil profile (i.e., silt loam topsoil with sandy loam subsoil) similar to the primary study field described above, and two are considered a sandy loam soil. These fields represent varying distances from the primary study field, with the two sandy loam fields being the farthest away.

https://doi.org/10.5194/egusphere-2025-2434
Preprint. Discussion started: 23 June 2025

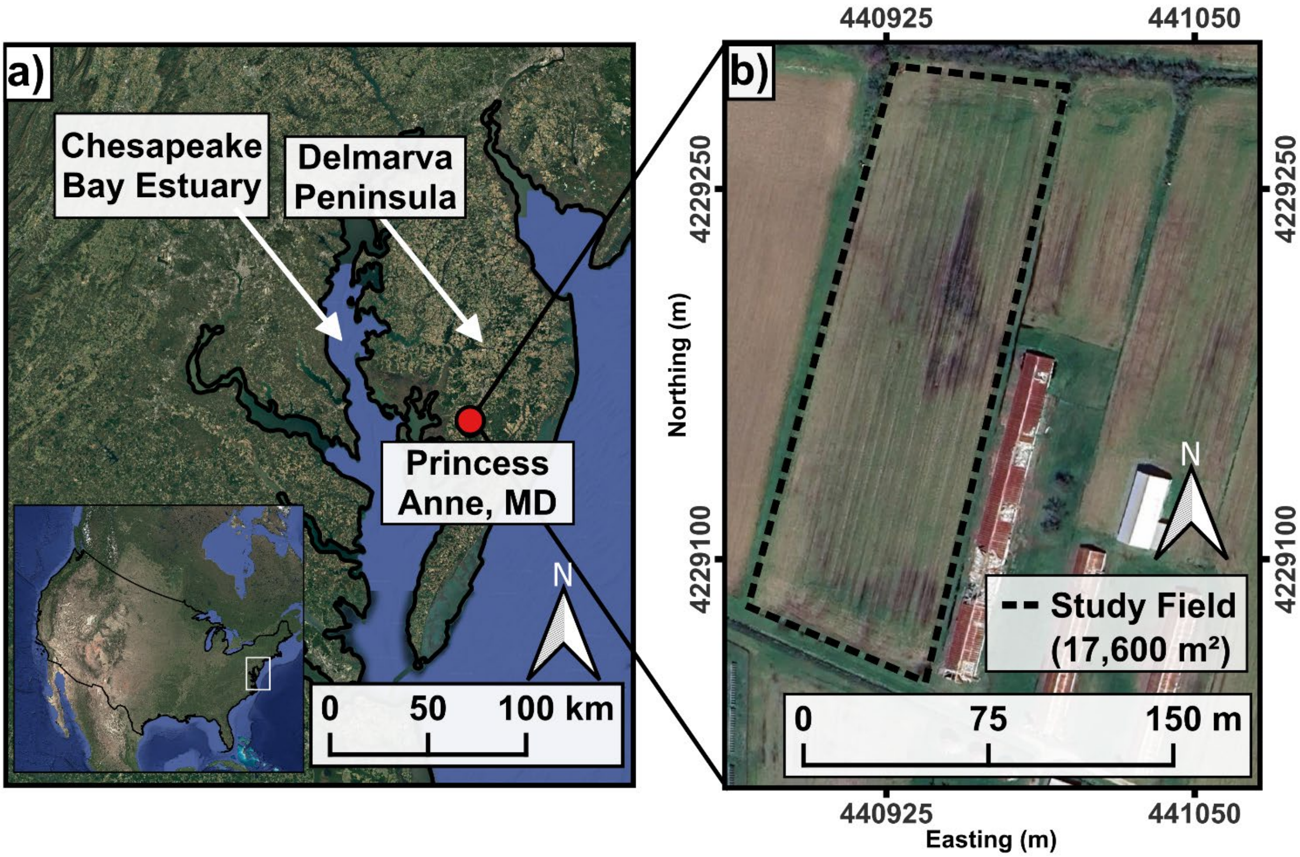

**Figure 2.** a) Chesapeake Bay and Delmarva Peninsula are located on the eastern coast of the United States (white box). Princess Anne, Maryland (MD) is located on the lower Delmarva. b) The dashed line is the primary study field, roughly 17 600 m$^2$.

The survey layout was designed to provide multiple, collocated observations to apply the CIC workflow (Fig. 1), including a field-scale EMI survey, two ERI profiles, and 10 soil cores to 3 m depth (Figure 3). The EMI survey was collected on October 11, 2019 with a Dualem 421S (Dualem; Ontario, Canada) that collected six simultaneous $\sigma_{a,\ EMI}$[nc] measurements using a frequency of 9000 Hz at 3,420 locations across the field (Fig. 3) resulting in just over 20,500 total measurements. The instrument has three horizontal coplanar (HCP) coils with 1, 2, and 4 m separations and three perpendicular coplanar (PRP) coils at 1.1, 2.1, and 4.1 m separations. The instrument was walked in every third plant row of the field, ~ 100 measurement locations per row, resulting in lines spaced ~1 m apart. Each measurement location was georeferenced using a Trimble SC2 with an accuracy of <1 m.

Two 2D ERI profiles were acquired on May 19, 2021, using a Syscal Pro/Switch resistivity instrument (Iris Instruments, Orleans, France). ERI Profile 1 has the first electrode on the northeast side with 94 electrodes in total, spaced 1 m apart. This profile crosses a region that is susceptible to significant surface runoff due to a less permeable topsoil, indicating that significant soil texture variations occur across the profile. ERI Profile 2 spanned from the first electrode on the east field edge to the west, with 77 electrodes spaced 1 m apart. The soil coring locations were guided by a preliminary inverted conductivity model from

140 the EMI survey, assuming that significant conductivity variations across the profile are primarily caused by soil textural changes. A direct push Geoprobe 6712DT drill rig was used to retrieve 10 minimally disturbed soil cores of 0.05 m diameter to 3 m depth. Four soil cores were acquired along ERI Profile 1 (S1-S4), three cores were acquired along ERI Profile 2 (N1-N3), and three additional cores were collected away from both ERI profiles (A1-A3).

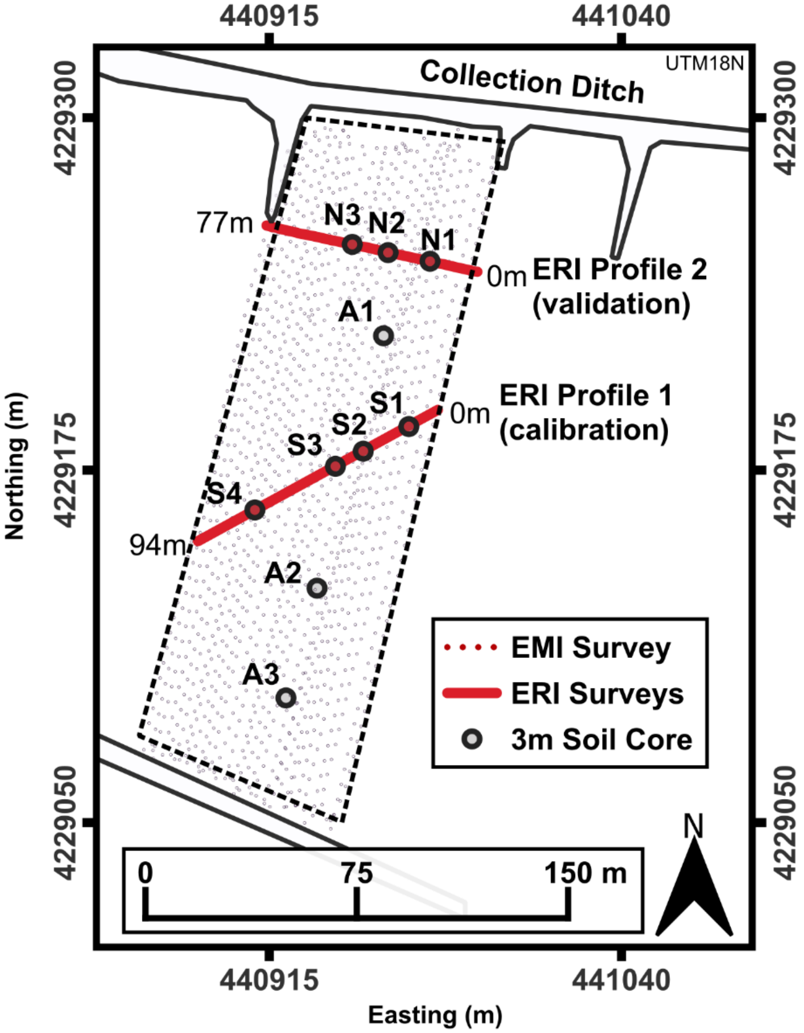

**Figure 3.** EMI survey (small circles) across the entire study field (black dashed line). The location of two ERI profiles are the red lines with electrode 1 located on the east side (0 m) in both cases. ERI Profile 1 was used for the calibration and ERI Profile 2 was used for validation of in CIC workflow (Fig. 1). Four soil cores are located along ERI Profile 1 (S1-S4) and three cores are along ERI Profile 2 (N1-N3). Three addition cores were collected away from the ERI profiles (A1-A3). All cores were drilled to 3 m depth. The white polygons to the north and south are artificial drainage ditches.

145

Figure 4 shows soil texture profiles along the location of ERI Profiles 1 and 2. Four soil texture ranges are represented: 1) silt, 2) silt loam - loam, 3) loamy sand to sandy loam, and 4) sand. The soil profiles contain fine textures within the top meter and progressively shift from loamy to sandy at depth. ERI Profile 1 (Figure 4b) shows the greatest soil texture variation amongst the two transects. Soil profile S2 contains two silt layers: one at the surface and the other between 1 m and 1.8 m. Gray soil, with a chroma ≤ 2 from the Munsell soil color chart, was observed at ~2.5 m depth, continuing until 3 m depth in the soil cores. The soil below 2.5 m depth is likely anaerobic due to periods of persistent saturation. While the water levels were not directly measured during the surveys, a chroma value ≤ 2 likely represents the seasonal-high water table at the site.

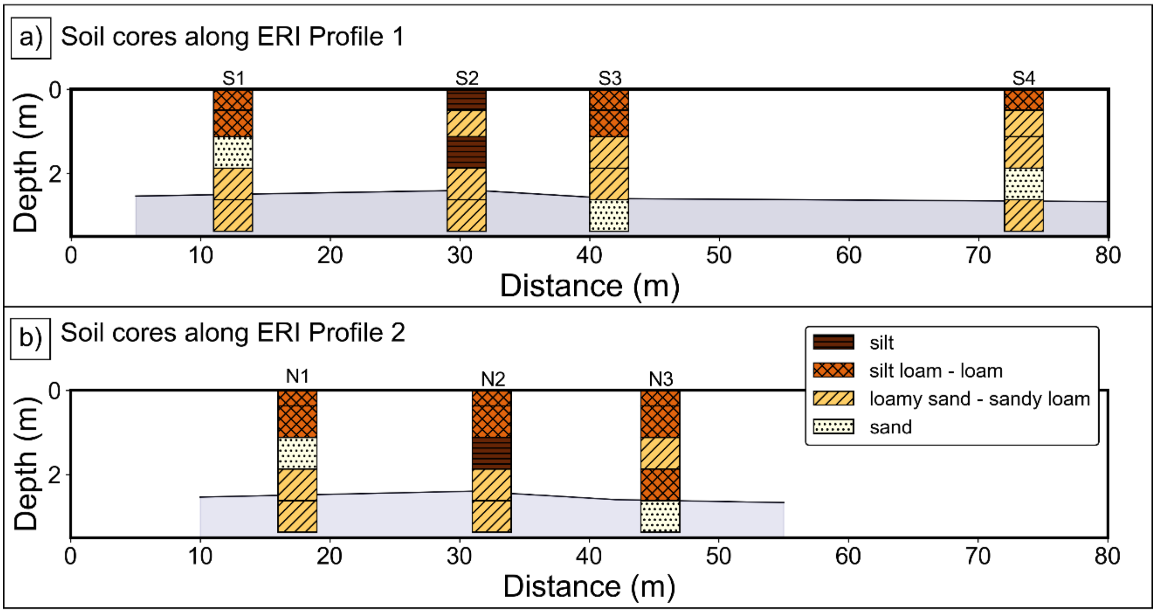

**Figure 4.** Soil texture along the four sampled cores along ERI Profile 1 (S1, S2, S3, S4) and three cores along ERI Profile 2 (N1, N2, N3). The soil textures are divided into four groups: silt, silt loam – loam, loamy sand – sandy loam, and sand. The light blue shaded region is the interpolated depth to the grey soil layer, suggesting persistent saturation after 2.5 m depth.

### 3.3 Pre-calibration: Electrical Resistivity Imaging (ERI)

Galvanic ERI surveys use electrodes inserted a few centimeters into the soil with current injected between one pair of electrodes, and the resulting voltage difference measured with another pair of electrodes. The ratio of the voltage drop and current is equal to the transfer resistance defined by Ohm's law. The transformation from transfer resistance to a subsurface conductivity model consistent with the data is performed via inverse modeling. The ERI inversion is an iterative process that minimizes an objective function composed of a data misfit and a model misfit term (Binley & Kemna, 2005).

In this study, a data acquisition sequence collected between 1200-1500 measurements, with ~43% containing reciprocals (i.e., where the current and electrodes are swapped, and a second measurement is taken). Von Hebel et al. (2019) found the dipole-dipole with short offset provided a better ERI model to use for calibration. We used a sequence that combines array types such as dipole-dipole with a short offset, nested dipole, and Wenner to provide high sensitivity (Mwakanyamale et al., 2012). ERI inversions were performed with the open-source code ResIpy (Blanchy et al., 2020), which calls the R2 family of scripts (Binley, 2015). An error model was developed using the reciprocal error as a function of transfer resistance (Koestel et al., 2008). The reciprocal error model only accounts for the errors associated with the acquisition of the measurements and does not consider the modeling errors that arise due to mesh discretization. Thus, a combination of the reciprocal and modeling errors was used to enforce a stronger agreement between higher-quality ERI measurements and simulated measurements. A depth of investigation (DOI) index was computed (Oldenburg & Li, 1999) to define regions of the ERI conductivity model to exclude from the analysis.

### 3.4 Electromagnetic induction

EMI instruments measure soil electrical conductivity by driving an alternating current through a coil to produce a time-varying primary magnetic field ($\mathbf{B}_p$) that induces eddy currents in the soil. The eddy currents induce a secondary magnetic field ($\mathbf{B}_s$) and the superposition of the two magnetic fields is recorded by the instrument. The ratio of $\mathbf{B}_s/\mathbf{B}_p$ is a complex expression where the in-phase component is sensitive to changes in magnetic susceptibility, while the out-of-phase component, or the quadrature (Q) component, is used to approximate apparent conductivity ($\sigma_{a,\,EMI}$) values (Boaga, 2017; for review). Given that the coil spacings at the instrument frequency satisfy the low induction number (LIN) criterion at our study sites, the $\sigma_{a,\,EMI}$ approximation is calculated using,

$$\sigma_{a,\ EMI} = \frac{4}{\omega\mu_0 s^2} Q$$

**Equation 1**

where $\omega$ is the frequency (Hz), $\mu_0 = 4\pi \times 10^{-7}\mathrm{H/m}$ is the magnetic permeability of free space, $s$ is the coil separation (m), and $Q$ is the quadrature term (McNeill, 1980). We used Eq. 1 to calculate $\sigma_{a,\,EMI}$ as induction numbers for all coil configurations were less than 0.04, being well below the threshold of 0.3, proposed by (Wait, 2012).

### 3.5 Filtering, Calibration, and Inversion of EMI data

The EMI data were filtered before the calibration, with $\sigma_a$ values falling outside of the range 1-50 mS/m were removed and a rolling mean applied that averaged every 2 data points. This range of $\sigma_a$ values is representative of a silt loam dominant fields and is consistent across multiple agricultural fields across the Delmarva. The filtering range is appropriate for these silt loam fields, considering the mean conductivity for the EMI measurements is ~8 mS/m.

Once the EMI measurements are filtered, a simulated apparent conductivity dataset ($\sigma_{a,\ sim}$[cal]) was created based on the EMI instrument's coil configurations and operating frequency, a set of layer thickness values, and the conductivity of those layers from $\sigma_{\mathrm{ERI}}$[cal] for Profile 1. Similar to Mclachlan et al. (2021), the EMI measurement coordinates were interpolated to a distance along the ERI electrode line, with an average distance of 1.5 m between the EMI and ERI coordinates. Depth-specific conductivity from $\sigma_{\mathrm{ERI}}$[cal] was used to create a total of 816 simulated model responses, with 136 for each of the six coil configurations. The slope and intercept from a localized linear regression between $\sigma_{\mathrm{a,\ sim}}$[cal] and co-located ($\sigma_{\mathrm{a,\ EMI}}$[nc]) of each coil configuration was applied to calibrate the entire 20,688 EMI measurements.

After the calibration, $\sigma_{\mathrm{a,\ EMI}}$[c] and $\sigma_{\mathrm{a,\ EMI}}$[nc] were inverted separately for a 7-layer model, with each layer's starting conductivity equal to 8 mS/, which is the average conductivity measured across all coil configurations. The first layer depth was 0.3 m, with each subsequent layer having a thickness of 1 m down to 6.3 m. The inversion seeks to find a simulated conductivity for the 7-layer model that minimizes an objective function,

$$\phi = \phi_{\mathrm{data}} + \alpha\phi_{\mathrm{model}}$$

**Equation 2**

where $\phi$ is the total misfit, $\phi_d$ is the data misfit, $\alpha$ is the regularization parameter, and $\phi_m$ is the model misfit.

The data misfit is defined as the $L_2$ norm between the EMI measurements ($d$) and the forward model ($m$) using the LIN approximation,

$$\phi_d = \frac{1}{N}\Sigma_{i=1}^{N}(d_i - m_i)^2$$

**Equation 3**

where $N$ is the number of coil configurations. The data misfit is a squared norm equal to zero when the simulated model equals observed data. Therefore, a lower data misfit indicates a greater similarity between the observed and simulated measurements. The model misfit ($\phi_m$) favors a conductivity model that changes smoothly with depth,

$$\phi_m = \frac{1}{M}\Sigma_{i=1}^{M}\left(m_j - m_{j+1}\right)^2$$

**Equation 4**

where $M$ is the number of layers and $\sigma_j$ is the conductivity of the layer. The $\alpha$ parameter can be chosen by plotting $\phi_d$ vs $\phi_m$ over a range of $\alpha$ values, known as the l-curve, where the ideal value of $\alpha$ is defined by the elbow of the curve. Overemphasizing the data misfit using a lower $\alpha$ value increases the likelihood of fitting noise, producing a conductivity model with significant uncertainty. However, a lower $\alpha$ value, away from the elbow of the l-curve, was necessary in this study to ensure minimal smoothing of the calibration effects, which masked the relationship with the vertical soil profiles (discussed later). The $\sigma_{\mathrm{a,\ EMI}}$[c] and $\sigma_{\mathrm{a,\ EMI}}$[nc] inversions were done with identical inversion parameters to assess the effect of the ERI-informed calibration.

https://doi.org/10.5194/egusphere-2025-2434
Preprint. Discussion started: 23 June 2025

### 3.6 Kling-Gupta Model Performance metric

One method used extensively for model validation in hydrology is the Kling-Gupta Efficiency (KGE), which is an aggregated performance metric that considers the correlation, prediction bias, and relative variability between simulated and observed hydrological model outputs (Gupta et al., 2009). The KGE is expressed as the Euclidean distance away from an ideal model that perfectly matches observations,

$$KGE = 1 - \sqrt{(r-1)^2 + \left(\frac{sim_{std}}{obs_{std}} - 1\right)^2 + \left(\frac{\widehat{sim}}{\widehat{obs}} - 1\right)}$$

**Equation 5**

Where r is the Pearson correlation coefficient, $\frac{sim_{std}}{obs_{std}}$ is the relative variability and $\frac{\widehat{sim}}{\widehat{obs}}$ is the ratio of means (or bias) from the simulated and observed data. The Pearson r correlation coefficient measures the strength and direction of a linear relationship between a simulated model and observed data. We use the KGE as a performance metric to compare the inverted conductivity models ($\sigma_{EMI}$[c] and $\sigma_{EMI}$[nc]) with the external validation datasets (electrical conductivity of soil cores, $\sigma_{ERI}$ from inversion of a separate profile) treated as observations. A higher KGE value, and reasonable values for *r*, relative variability, and bias, will indicate whether $\sigma_{EMI}$[c] or $\sigma_{EMI}$[nc] matches more closely with the observation data. In some cases, the EMI conductivity model could be highly correlated to the observed data (high Pearson *r*) and yet still systematically over- or under-predict the observed data, indicated with a bias value not equal to 1 in Eq. 5. The relative variability determines how closely the range of conductivity values in the EMI conductivity model matches the spread of the observed data (Gupta et al., 2009). The KGE value can range from $-\infty$ to 1, where a KGE=1 represents a perfect match between observations and conductivity models.

### 3.7 KGE using core-scale conductivity

Electrical conductivity measured on soil cores provided true, depth-specific measurements rather than an average, depth-weighted EMI or ERI soil conductivity measurement. To remove the effects of variably saturated soils, measurements were obtained under fully saturated conditions using synthetic groundwater with a constant, low fluid conductivity (0.1 mS/m) to evaluate the soil texture controls on the core-scale electrical conductivity. The fluid conductivity of the synthetic groundwater reflects that of the regional groundwater fluid conductivity and significant groundwater salinization is not assumed to occur on the farm. Both ends of the 0.13 m core were equipped with leakproof end caps, and the interior of both end caps contained a coiled copper wire used to transmit an electrical current through the soil. Two potential electrodes penetrated the casing on the side of the core to measure the voltage drop (Wang & Slater, 2019). The greatest measurement uncertainty in the field-scale EMI surveys is below 2.5 m depth that are likely more highly influenced by moisture content. Therefore, the core-scale measurements were conducted on the last 0.13 of the 3 m depth soil cores to capture conductivity likely from texture variation, given the known saturation and low fluid conductivity.

https://doi.org/10.5194/egusphere-2025-2434
Preprint. Discussion started: 23 June 2025

### 3.8 KGE using ERI profile unseen to calibration step

A split-location validation was applied by computing the KGE between $\sigma_{ERI}$ from ERI Profile 2 and collocated conductivity values from $\sigma_{EMI}$[c] that were not used in the calibration. The data split resulted in 55% (ERI Profile 1) of the total data allocated for the calibration and 45% (ERI Profile 2) used for validation. The KGE using ERI Profile 2 evaluated how well $\sigma_{EMI}$[c] (and $\sigma_{EMI}$[nc] for comparison) represents electrical conductivity structure away from the calibration site. Thus, the validation process across soil data, core-scale, and field-scale electrical measurements provided a detailed evaluate the ability of $\sigma_{EMI}$[c] to represent soil texture variations and the geoelectrical signatures of those fine-textured soils across the field site.

### 3.9 Non-parametric KGE: grain size and $\sigma_{EMI}$

Assessment of the correlation between the non-normal grain size distributions and $\sigma_{EMI}$[c] and $\sigma_{EMI}$[nc] required a non-parametric approach appropriate for non-uniform data. Thus, a non-parametric KGE (denoted as $KGE_{np}$) that does not require the condition of normally distributed data was applied, by replacing Pearson r with Spearman's r. A relative variability term that does not depend on a normal distribution was used to represent variability across all grain sizes, focusing less on grain size variability around the mean. Under similar saturated conditions, soil grain size can strongly influence conductivity measurements due to surface conduction effects increasing with high surface area associated with fine-grained particles. Therefore, we established an empirical relationship between electrical conductivity and representative grain diameter, defining sizes for which a certain percent of the sample is finer by volume ($d_{finer}$). For brevity, only the Spearman's r is shown in the results section. The non-parametric KGE analysis between grain size and $\sigma_{EMI}$ is shown in the supplemental data (Supplemental Figure 1).

## 4 Results

### 4.1 Pre-calibration: inverted ERI conductivity models

Figure 5 shows the inverted conductivity models $\sigma_{ERI}$ with DOI index contour for each shown. Soil core locations along each profile are also shown. The values (in white text) at 3 m depth along each profile are the electrical conductivity from the core-scale measurements described in Section 3.8. Both profiles show a consistent low conductivity layer just below 1.5 m extending to ~2.5 m and a higher conductivity zone just below 2.5 m in depth. ERI Profile 1 (Fig. 5a) has higher conductivity values below 2.5 m in depth relative to ERI Profile 2, which has a discontinuous conductivity layer. The core-scale conductivity values support the conclusion that higher conductivity values are found along ERI Profile 1. Indeed, the highest conductivity values from the core-scale measurements across all 10 samples are along ERI Profile 1, with core-scale conductivity values for A1-A3 (not shown in Fig. 5) being less than 9 mS/m. The conductivity structure from Fig. 5a-5b is likely related to textural variations rather than variable moisture content or changes in fluid conductivity since the core-scale measurements, which were under completely saturated conditions with a constant fluid conductivity, agree with variations observed at the field scale.

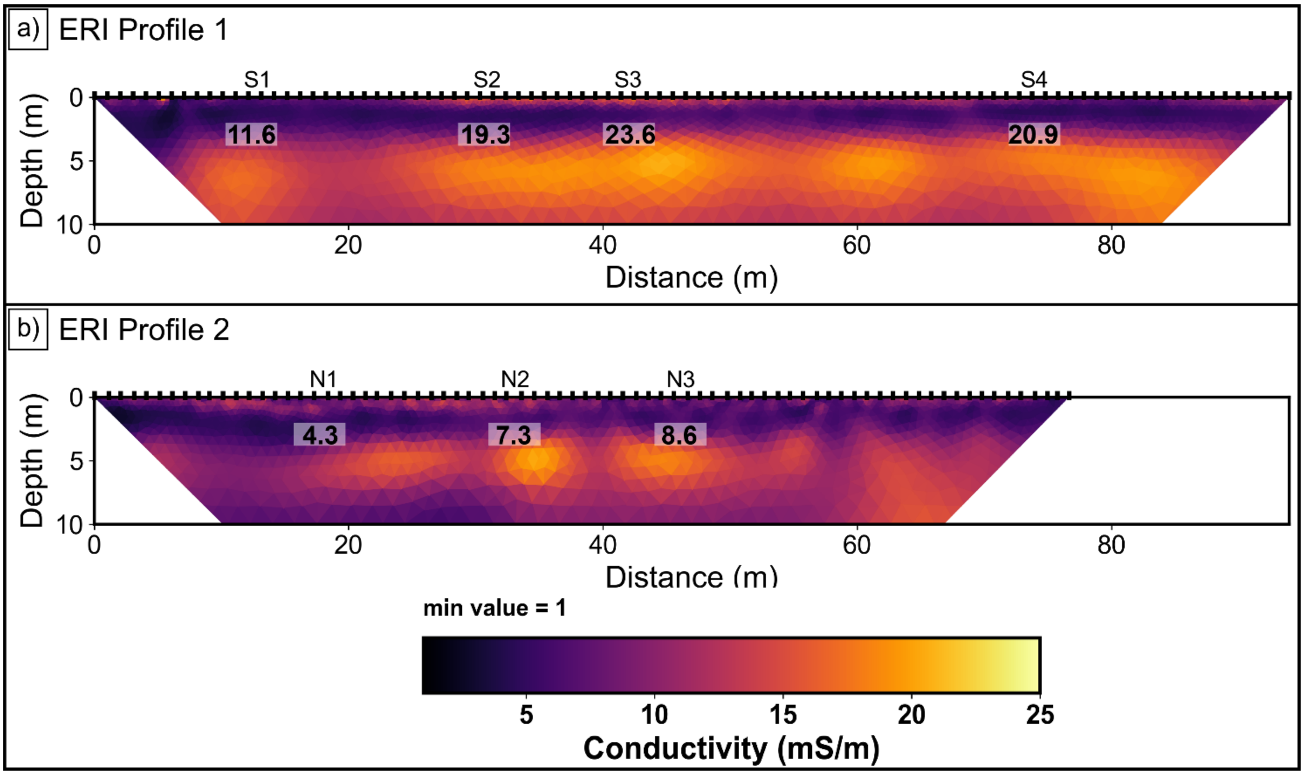

**Figure 5.** a) Inverted conductivity model for Profile 1 ($\sigma_{ERI}$[cal]). b) Inverted conductivity model for Profile 2 ($\sigma_{ERI}$[val]). The numbers at 3 m depth along a) and b) correspond to the electrical conductivity measurements of each soil sample at 3 m depth in units of mS/m. The soil coring locations along ERI Profile 1 are defined as S1, S2, S3, and S4 in frame a) and the soil sampling locations along ERI Profile 2 are defined as N1, N2, and N3) in frame b).

### 4.2 Calibration and inversion of EMI data

The calibration of the EMI dataset against the conductivity model from the ERI profile is shown in Figure 6 for the six measurements (pairs of coils) used by the Dualem. The regression line (red dashed line) overlays each plot, and the coefficient of determination ($R^2$), slope, and y offset are displayed. Figure 6a-6c shows that the HCP coils measure higher $\sigma_{a,EMI}$[nc] values relative to the simulated $\sigma_a$, while the PRP coils tend to measure lower $\sigma_{a,EMI}$[nc] relative to the simulated $\sigma_a$. The HCP1.0 and PRP 1.1 coil configurations have the lowest $R^2$ values, likely because of the increased noise with short offset coil separations. The HCP 2.0, PRP 2.1, and PRP4.1 configurations have measured $\sigma_{a,EMI}$[nc] values that lie the closest to the 1:1 line with the simulated $\sigma_a$, indicating high sensitivity to subsurface conductivity features.

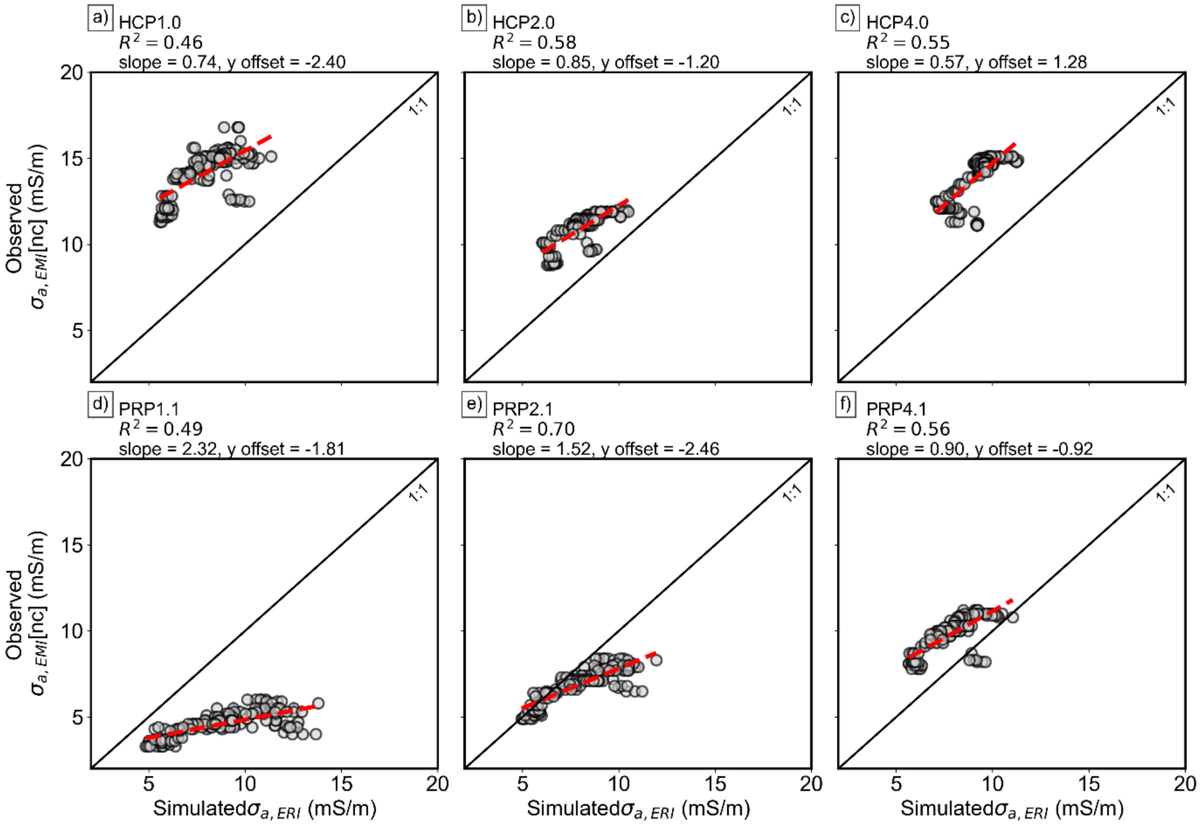

**Figure 6.** EMI measurements $\sigma_{a,\mathrm{EMI}}$[nc] versus simulated apparent conductivity $\sigma_a$ based on the inverted conductivity model from ERI Profile 1 for each of the six coil configurations. The red line is the regression line. Regression slope and y-offset (mS/m), as well as $R^2$, values are shown. The first row (6a-6c) represents the HCP coils, and the second row (6d-6f) represents the PRP coils.

Figures 7a - 7f show the data misfit plots and root mean square error (RMSE) for simulated EMI data for the final inverted EMI model and the measurements when uncalibrated ($\sigma_{a,\mathrm{EMI}}$[nc]) and calibrated ($\sigma_{a,\mathrm{EMI}}$[c]) data are inverted. The RMSE for the three HCP coil separations (Fig. 7a-7c) is reduced by 3 to 8 times for $\sigma_{a,\mathrm{EMI}}$[c] compared to $\sigma_a$[nc]. Figure 7d-7f shows that the RMSEs for the PRP coil separations are also reduced by a factor of ~1.5, except for PRP2.1 (Fig. 7e) when comparing $\sigma_{a,\mathrm{EMI}}$[c] to $\sigma_{a,\mathrm{EMI}}$[nc].

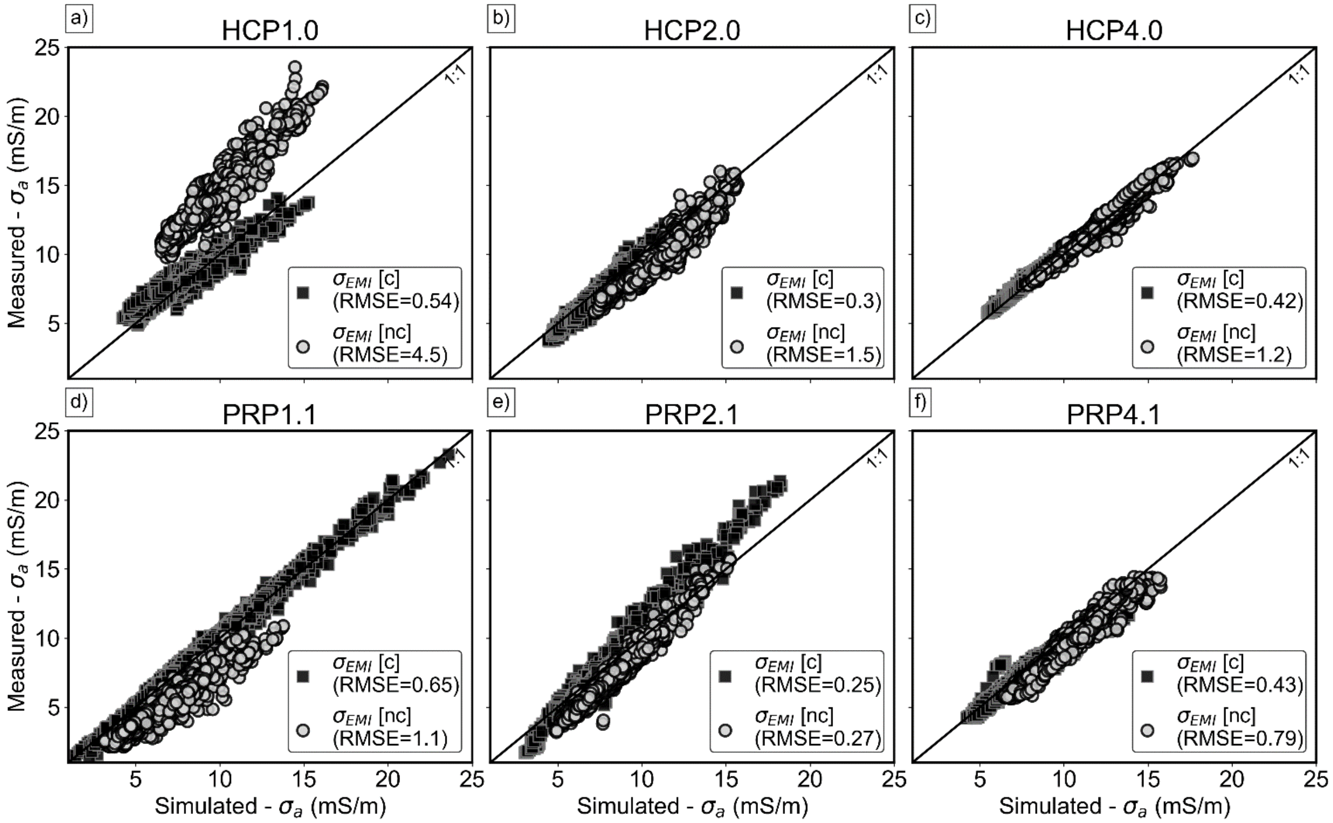

**Figure 7.** a) – f) Measured EMI data versus simulated EMI data based on the final EMI model from the inversion when uncalibrated ($\sigma_{a,\,EMI}$[nc]) and calibrated ($\sigma_{a,\,EMI}$[c]) measured data are inverted. Data shown for all six coil configurations.

### 4.3 Comparison

#### 4.3.1 Comparing conductivity models with grain size

We compare the differences in Spearman r between the soil electrical conductivity from the EMI inversions and percent finer classes into $d_{10}$, $d_{30}$, $d_{60}$, and $d_{90}$ across all samples. As mentioned in section 3.7, the correlations were computed in $\log_{10}$ space, and the linear values are displayed on Figure 8. Cross-plots with a regression line (red) are shown for co-located soil conductivity values extracted from $\sigma_{EMI}$[c] (Fig. 8a-8d) and from $\sigma_{EMI}$[nc] (Fig. 8e-8h). The symbols are colored by depth to provide a clearer spatial context. The $\sigma_{EMI}$[nc] values have no significant correlation with any $d_{finer}$ class, and the highest correlation magnitude occurs with $d_{10}$ (Spearman r=-0.297). A striking result of the effect of the EMI calibration is highlighted in Fig. 8a-8d, with marked increases in correlations between all $d_{finer}$ classes and $\sigma_{EMI}$[c]. Figure 8a shows that the highest correlation is observed for $d_{10}$ (Spearman r=-0.608). Similar to the cross-plots for $\sigma_{EMI}$[nc], the slope of the regression line decreases as the grain sizes increases; however, the trend is significantly subdued. Figure 8 shows that the calibration is necessary to recover the expected trend of decreasing grain size with increasing soil conductivity.

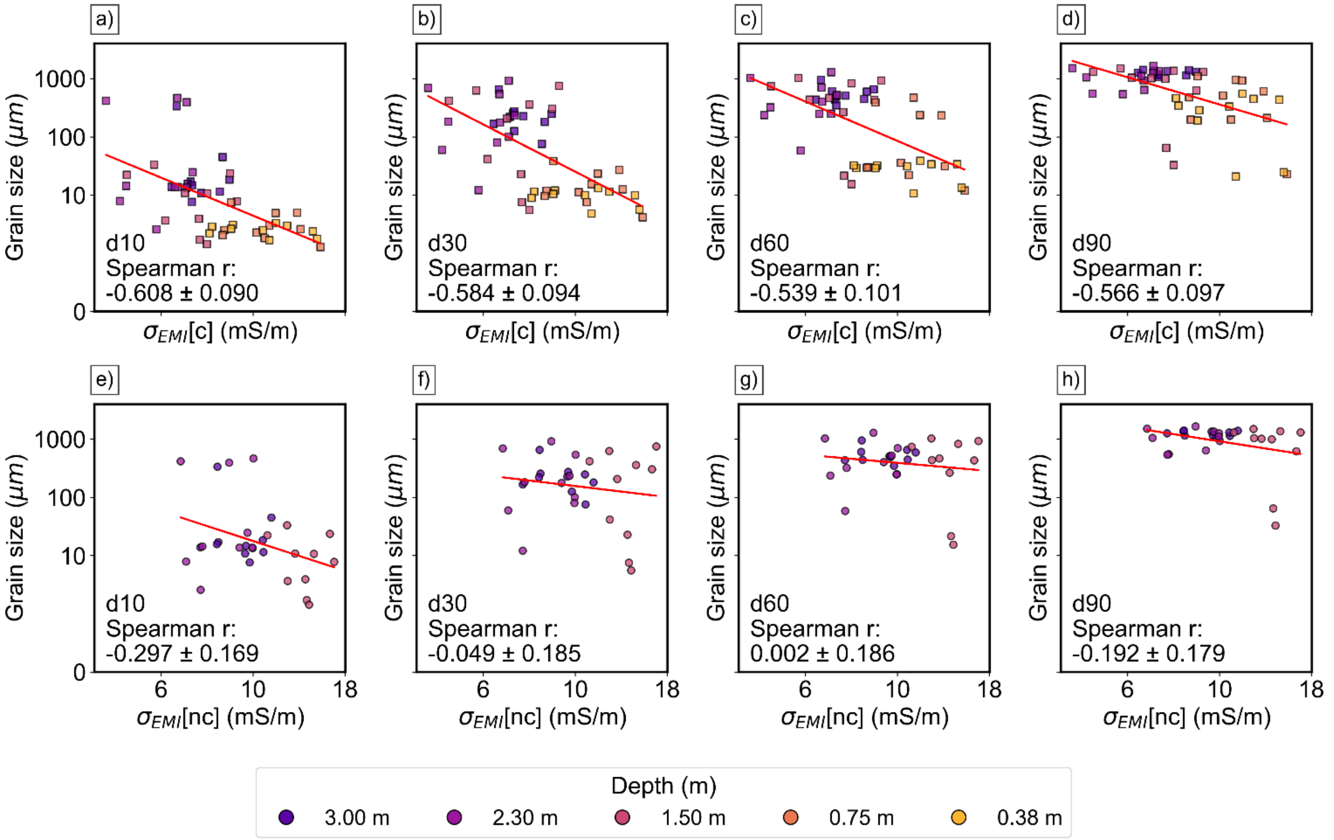

**Figure 8.** Cross plots and linear regressions showing the relationship between grain size and electrical conductivity for inversions of calibrated (a-d) versus not calibrated (e-h) EMI datasets. The Spearman r with an uncertainty is shown for each cross plot. The symbol color is defined by depth to provide a lithological context.

### 4.3.2 Core-scale conductivity

Figure 9a shows cross plots between the conductivity measured on soil cores and the $\sigma_{EMI}$[c] (Fig. 11a), and $\sigma_{EMI}$[nc] (Fig. 9b), with the KGE results displayed. There is a significant improvement to the correlation with $\sigma_{EMI}$[c] and the core-scale conductivity measurements, having r=0.929 and $\sigma_{EMI}$[nc] having a correlation of r=0.79. Interestingly, there are no significant differences between $\sigma_{EMI}$[c] and $\sigma_{EMI}$[nc] for the bias and relative variability compared to core-scale conductivity measurements. Considering the core-scale conductivity values were measured under fully saturated conditions, we expected these values to be higher relative to field measurements under drier conditions. The bias and relative variability are predominantly influencing the lower KGE value for $\sigma_{EMI}$[c] (KGE=0.194) relative to $\sigma_{EMI}$[nc] (KGE=0.231). This is likely a result of comparing conductivity measurements with different moisture content and different measurement volumes. However, with similar bias and relative variability estimates, the results imply that $\sigma_{EMI}$[c] has a superior ability to predict the core-scale conductivity values because of a high Pearson r correlation compared to $\sigma_{EMI}$[nc].

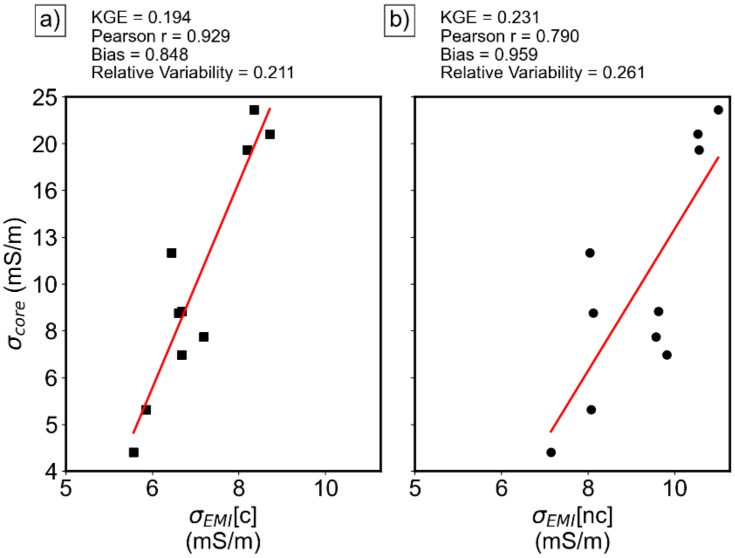

**Figure 9.** Cross plot between the core-scale conductivity from 3 m depth, with (a) $\sigma_{EMI}$[c] and (b) $\sigma_{EMI}$[nc] with a linear regression line overlayed. The KGE statistics are displayed above each graph for comparison.

### 4.3.3 Split-location validation comparison to ERI Profile 2

We investigated the calibration effects on EMI conductivity models for Profile 2 when compared to the inverted ERI conductivity for this profile. Figure 10a shows the probability density function of the prediction error between $\sigma_{ERI}$ and the calibrated and uncalibrated EMI conductivity models. Notably, the prediction error is centered about zero for $\sigma_{EMI}$[c], indicating a substantial similarity between $\sigma_{EMI}$[c] and $\sigma_{ERI}$[val]. The spread of the prediction errors is also reduced for $\sigma_{EMI}$[c] compared to $\sigma_{EMI}$[nc]. Indeed, the $\sigma_{EMI}$[nc] tends to overpredict $\sigma_{ERI}$[val], with a greater variability of prediction errors.

Figure 10b-10c shows the cross plots between the EMI conductivity models and $\sigma_{ERI}$[val] from ERI Profile 2, along with the KGE statistics. Similar to Fig. 8, the symbols are colored by depth to provide an additional view of the spatial relationships between the EMI and ERI conductivity models. The depth to specific conductivity values is aligned with the site conceptual model of a fine-textured topsoil (yellow symbols) and a sandy subsoil (orange symbols at 3 m depth). Beyond the depths of the soil cores, the conductivity from the EMI and ERI shows that the conductivity increases between 3- and 7-meter depths. Generally, the calibration adjusts the inverted EMI conductivity to lie along the 1:1 line with the collocated ERI Profile 2 conductivity, supporting the observation that the prediction errors are reduced in Fig. 10a. The $\sigma_{EMI}$[c] has a higher KGE (KGE=0.632; Fig. 10a) relative to the $\sigma_{EMI}$[nc] (KGE=0.32; Fig. 10b). There is a substantial improvement for the calibration of EMI data to recover a conductivity structure from additional ERI Profiles at least 80 m away from the calibration locations.

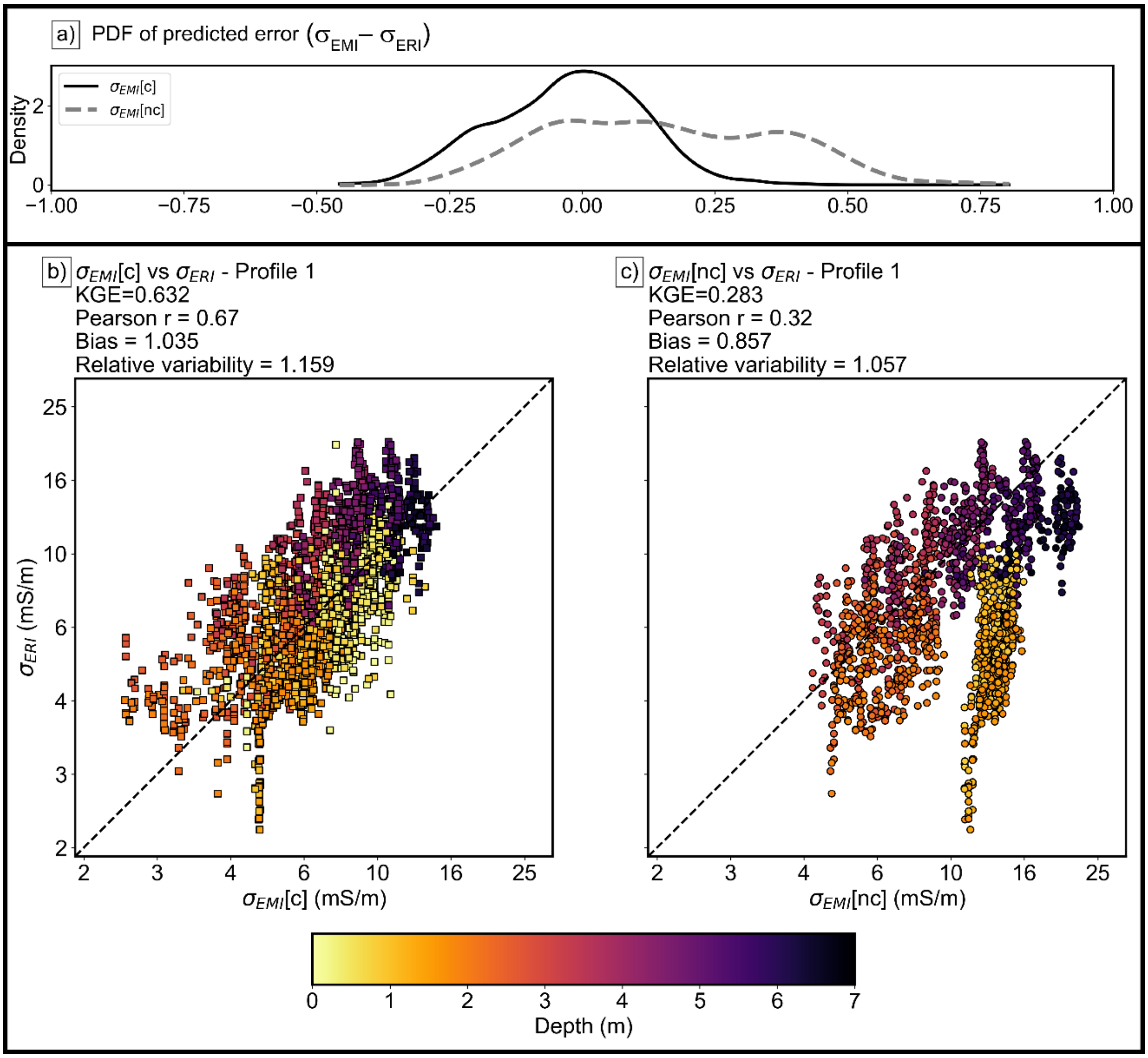

**Figure 10.** a) Prediction error between $\sigma_{ERI}$[val] values and values of $\sigma_{EMI}$[c] and $\sigma_{EMI}$[nc] with the x-axis representing the difference between the $\sigma_{EMI}$ and $\sigma_{ERI}$[val]. Cross plots comparing the differences between $\sigma_{EMI}$[c] (b) and $\sigma_{EMI}$[nc] (c) with the inverted conductivity $\sigma_{ERI}$ from ERI Profile 2. The symbols are colored by depth to emphasize the spatial differences between $\sigma_{EMI}$[c] and $\sigma_{EMI}$[nc].

## 5 Discussion

This study emphasizes the benefits of calibrating $\sigma_{a,\ EMI}$ against ERI conductivity models for reliable estimates of lateral and vertical soil texture variations at the field scale. The $\sigma_{a,\ EMI}$[nc] required calibration since the data significantly deviated from the 1:1 line with $\sigma_{a,\ sim}$[cal] (Fig. 6). The inversion of $\sigma_{a,\ EMI}$[c] showed a reduced RMSE of the data misfit for all coil configurations relative to the inversion of $\sigma_{a,\ EMI}$[nc]. Such reduction in error in the data misfit of $\sigma_{EMI}$[c] has been observed across various inversion routines (Mester et al., 2011; von Hebel et al., 2014; Von Hebel et al., 2019). Overall, the calibration of EMI data and subsequent inversion produced a conductivity model that agreed with grain size distributions, core-scale conductivity measurements, and $\sigma_{ERI}$[val] for the primary study field.

A comparison between $\sigma_{EMI}$[c] and depth-specific $d_{finer}$ classes (relative to the equivalent comparison with $\sigma_{EMI}$[nc]) demonstrated that the calibration was indispensable to establishing a relationship between $\sigma_{EMI}$[c] and soil texture. Figure 10a suggests a higher correlation of $\sigma_{EMI}$[c] with the finest and coarsest fractions of the grain size distributions. The greater agreement between the $\sigma_{EMI}$[c] and smaller grain sizes is comparable to recent soil studies comparing EMI inverse models with clay fractions. O'Leary et al. (2024) reported a significant Pearson correlation (r=0.87) between inverted EMI conductivity and clay fractions to a depth of ~1.2 m depth in sandy loam agricultural fields using inverted clusters of the apparent conductivity as a starting model for the EMI inversion. Khongnawang et al. (2019) reported a similar Pearson r (r=0.80) when comparing $\sigma_{EMI}$ and clay content down to ~1 m depth in sandy loam to sandy soils. When considering the similarities with additional ERI surveys, there was a significant spatial correlation with $\sigma_{EMI}$[c] and a second ERI Profile ($\sigma_{ERI}$[val]) 80 m away from the calibration site. Similarly, Von Hebel et al. (2014) found a greater visual agreement between an ERI-informed calibration of inverted EMI measurements with two independent ERI profiles. Zaru et al. (2023) validated the calibrated and inverted EMI measurements by observing similar subsurface structures in GPR radargrams and borehole stratigraphy logs.

The current study stands apart by demonstrating the $\sigma_{EMI}$[c] has a significantly stronger and more physically meaningful relationship with lateral and vertical variations in soil texture compared to $\sigma_{EMI}$[nc]. When the smoothing parameter was set to $\alpha = 0.01$, the RMSE for the data misfit for $\sigma_{EMI}$[c] was reduced by half in most cases and also yielded higher Spearman's r values with $d_{finer}$. EMI inversions were repeated 173 times with an initial $\alpha = 0.001$ and incrementing the $\alpha$ value by 0.005 to understand how the correlation between $\sigma_{EMI}$[c] and grain size parameters are influenced by the smoothing. Spearman's r was computed between the inverted conductivity and six percent finer values ($d_5$, $d_{10}$, $d_{30}$, $d_{50}$, $d_{90}$, and $d_{95}$) for each value of $\alpha$. Results of this analysis can be found in the supplemental material (Supplemental Figure 2). At $\alpha = 0.03$, Spearman r is not statistically significant (p-value<0.005) between $\sigma_{EMI}$[c] and the percent finer values. Below $\alpha = 0.01$, the inversion seems to fit a larger portion of the noise and produces an increased number of nonphysical values for the inverted conductivity. Therefore, a value of $\alpha = 0.01$ balanced a statistically significant relationship with grain size that provided enough smoothing to reduce fitting noise.

The calibration improvements to the EMI data is validated against the independent ERI inverted conductivity model ($\sigma_{ERI}$[val]) based on statistical metrics of model performance using the KGE. The KGE between the $\sigma_{EMI}$[c] and $\sigma_{ERI}$[val] show a high correlation with a biased and relative variability close to 1, providing high confidence in the ability of the inverted EMI conductivity models to predict the electrical structure away from a calibration site. The KGE was also higher between the ERI conductivity model used for EMI measurement calibration ($\sigma_{ERI}$[cal]) and $\sigma_{EMI}$[c] compared to $\sigma_{EMI}$[nc]. This likely indicates that the $\sigma_{EMI}$[c] preserves localized conductivity structure from $\sigma_{ERI}$[cal] that is representative of the full range of soil heterogeneity across the entire agricultural field. Therefore, this study underscores the need to calibrate EMI measurements with ERI conductivity models to improve the relationship between soil texture and soil electrical conductivity measured from EMI instruments.

### 5.1 Applications beyond single field surveys

Larger scale application of localized calibration equations for EMI surveys, based on measurements of pore-fluid conductivity at a single site, has shown promise for large-scale investigations in agricultural soil salinity studies (Farzamian et al., 2019; Selim et al., 2025). Similarly, Kelley et al. (2017) discuss the need to catalog and share calibration equations or machine learning algorithms that quantitatively compare EMI surveys across a region for soil texture mapping. In this study, we evaluated if the calibration equations developed in the primary study field can be applied to regional EMI surveys on additional fields. Figure 11 comprises the seven calibrated EMI surveys across agricultural fields (with the primary study field included) on the Delmarva as describe in Section 3.2. The Marion Station, MD box plot with the blue asterisk is considered the most saturated site due to a large rainfall event the prior day. The mean and median inverted conductivity for the primary study field is larger than the silt loam fields, except for the highly saturated Marion Station, MD field. This suggests that the primary study field contained a higher portion of fine-textured soils compared to the silt loam fields and suitable for application to other fields with a smaller range of fine-textured soils (i.e., lower range of conductivity values). The calibration equations (Fig. 6) were applied to the seven EMI surveys on each field and then individually inverted. There is a reduction in the RMSE of data misfit for $\sigma_{EMI}[c]$ for each of the six fields, compared to $\sigma_{EMI}[nc]$. Notably, the silt loam fields have strikingly similar conductivity ranges after the calibration, as indicated by the whiskers of the box plots. Marion Station, MD, had visible surface water during the collection of the EMI data and reflects different field conditions compared to the other silt loam fields. This probably suggests that for the calibration equations to provide multi-field comparisons, the EMI surveys should be collected under similar saturation conditions. The other two field sites are sandy loam soils with lower mean conductivity and greater conductivity variation. Although these fields are considered sandy loam, it is noted that this region contains a larger amount of soil series within each field, as observed from the SSURGO soil maps. Thus, the calibration may not be as applicable to other fields with a different dominant soil type or if the variations in soil texture are greater than the field where the calibration equations were developed. It is likely that a few sites representative of each dominant soil type from the region should be used to develop calibration equations for each dominant soil type.

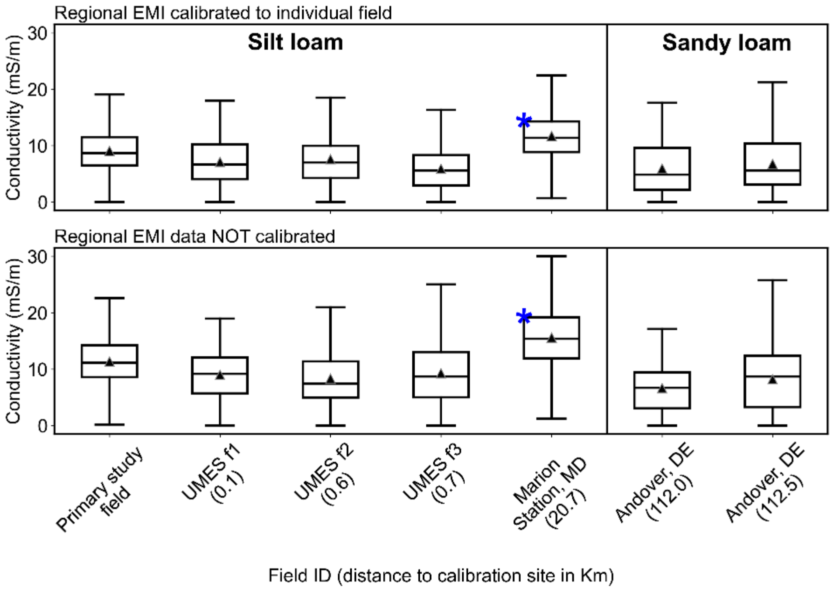

**Figure 11.** Results of applying the ERI calibration equation derived for the primary study field to EMI data collected in an additional seven fields. Plots show distributions of inverted conductivity ($\sigma_{EMI}[c]$) following inversion of calibrated EMI data (top) to distributions of inverted conductivity ($\sigma_{EMI}[c]$) following inversion of uncalibrated EMI data (bottom). The blue asterisk represents a field at saturated conditions during the time of the survey. The distance from the primary field site is reported under the field ID.

## 6 Conclusion

This study emphasizes the ERI-informed calibrations on EMI measurements vastly improves the quantitative relationship with grain size across a field and vertically to 3 m depth. The multi-coil EMI instruments are capable of measuring conductivity at the greater depths, taking a similar time to survey a field compared to EMI instruments with a single coil or short coil separations. Our approach suggests the possibility of extending the calibration equations beyond a single agricultural field. When applied under similar saturation conditions, the calibration equations from the primary field applied to six regional sites with similar dominant soils show remarkably consistent conductivity distributions. Additionally, the use of validation schemes, such as the KGE, or other metrics commonly reported in hydrological modeling studies, are transferable to electrical conductivity inverse models and should be used. A robust calibration-inversion-comparison (CIC) workflow can significantly increase the confidence of EMI surveys to be used with other remotely sensed or directly sampled data to predict soil-texture variation. In regions where transport of nutrients is primarily within subsurface groundwater flow, a deeper subsurface characterization by the calibrated EMI surveys can provide soil maps that consistently identify regions of texture-driven nutrient transport across multiple fields. The characterization of deeper soil structures can enhance our understanding of the hidden hydrologic connectivity to nearby surface waters. In low-relief, artificially drained agroecosystems on the Delmarva, upwards of 90% of Phosphorus is transported from agricultural fields to nearby surface waters via subsurface pathways (Kleinman, Peter J. A. et al., 2015). Thus, it is critical to characterize the lateral and vertical soil structures that may control nutrient transport. The calibrated EMI inversions, with robust validation schemes, can aid nutrient management across scales by revealing the deeper subsurface soil variations that tend to govern groundwater transport of agricultural nutrients.

**AUTHOR CONTRIBUTIONS:**

Joshua Thompson: Conceptualization, Data Curation, Formal Analysis, Investigation, Methodology, Supervision, Validation, Visualization, Roles/Writing – Original Draft, Writing – Review & Editing. Dimitris Ntarlagiannis: Conceptualization, Investigation, Methodology, Project Administration, Resources, Supervision, Validation, Writing – Review & Editing. Lee D. Slater: Conceptualization, Funding Acquisition, Investigation, Methodology, Project Administration, Resources, Supervision, Validation, Writing – Review & Editing.

**ACKNOWLEDGEMENTS**

The National Institute of Food and Agriculture's Agriculture and Food Research Initiative (AFRI) Project funded this work under Project #2019-68016-29405. Additional support was provided by USDA-ARS's Pasture Systems and Watershed Management Research Unit, Rutgers University Newark, the University of Delaware, and the University of Maryland Eastern Shore (UMES). We gratefully acknowledge Terry Troutman, Shawn Tingle, and Amy Collick for assistance with fieldwork. We thank Earle Canter for coordinating field activities and helping maintain the research site at the UMES Research and Teaching Farm.

**DECLARATION OF INTERESTS:** The authors declare no conflict of interest.

## References

Abdu, H., Robinson, D. A., Seyfried, M., & Jones, S. B. (2008). Geophysical imaging of watershed subsurface patterns and prediction of soil texture and water holding capacity. *Water Resources Research, 44*(4)10.1029/2008WR007043

https://doi.org/10.5194/egusphere-2025-2434
Preprint. Discussion started: 23 June 2025

Abdu, H., Robinson, D. A., Boettinger, J., & Jones, S. B. (2017). Electromagnetic induction mapping at varied soil moisture reveals field-scale soil textural patterns and gravel lenses. *Frontiers of Agricultural Science and Engineering, 4*(2), 135–145.

Allen, T. H. (2009). The transformation of forest and marsh in the agricultural landscape of the Lower Delmarva Peninsula. *Geocarto International, 24*(1), 37–46. 10.1080/10106040802069706

Binley, A. (2015). Tools and techniques: Electrical methods. *Treatise on Geophysics,* , 233–259.

Binley, A., & Kemna, A. (2005). DC resistivity and induced polarization methods. *Hydrogeophysics* (pp. 129–156). Springer.

Bjørn Møller, A., Koganti, T., Beucher, A., Iversen, B. V., & Greve, M. H. (2021). Downscaling digital soil maps using electromagnetic induction and aerial imagery. *Geoderma, 385*, 114852. 10.1016/j.geoderma.2020.114852

Blanchy, G., Saneiyan, S., Boyd, J., Mclachlan, P., & Binley, A. (2020). ResIPy, an intuitive open source software for complex geoelectrical inversion/modeling.

Boaga, J. (2017). The use of FDEM in hydrogeophysics: A review. *Journal of Applied Geophysics, 139*, 36. 10.1016/j.jappgeo.2017.02.011

Brogi, C., Huisman, J. A., Pätzold, S., von Hebel, C., Weihermüller, L., Kaufmann, M. S., van der Kruk, J., & Vereecken, H. (2019). Large-scale soil mapping using multi-configuration EMI and supervised image classification. *Geoderma, 335*, 133–148. 10.1016/j.geoderma.2018.08.001

Chardon, W. J., & Schoumans, O. F. (2007). Soil texture effects on the transport of phosphorus from agricultural land in river deltas of Northern Belgium, The Netherlands and North-West Germany. *Soil use and Management, 23*, 16–24. 10.1111/j.1475-2743.2007.00108.x

Christiansen, A., Pedersen, J. B., Auken, E., Søe, N. E., Holst, M. K., & Kristiansen, S. M. (2016). Improved Geoarchaeological Mapping with Electromagnetic Induction Instruments from Dedicated Processing and Inversion. *Remote Sensing, 8*(12)10.3390/rs8121022

Decker, L., Sawyer, A. H., Welch, S. A., Zhu, J., Binley, A., Field, H. R., Hanrahan, B. R., & King, K. W. (2024). Wide-ranging timescales of subsurface phosphorus transport from field to stream in a tile drained landscape. *Journal of Hydrology, 635*, 131185. 10.1016/j.jhydrol.2024.131185

Du, X., Jian, J., Du, C., & Stewart, R. D. (2022). Conservation management decreases surface runoff and soil erosion. *International Soil and Water Conservation Research, 10*(2), 188–196.

Farzamian, M., Paz, M. C., Paz, A. M., Castanheira, N. L., Gonçalves, M. C., Monteiro Santos, F. A., & Triantafilis, J. (2019). Mapping soil salinity using electromagnetic conductivity imaging—A comparison of regional and location-specific calibrations. *Land Degradation & Development, 30*(12), 1393–1406. 10.1002/ldr.3317

Friedman, S. P. (2005). Soil properties influencing apparent electrical conductivity: a review. *Computers and Electronics in Agriculture, 46*(1), 45–70. 10.1016/j.compag.2004.11.001

Fuchs, J. W., Fox, G. A., Storm, D. E., Penn, C. J., & Brown, G. O. (2009). Subsurface Transport of Phosphorus in Riparian Floodplains: Influence of Preferential Flow Paths. *Journal of Environmental Quality, 38*(2), 473–484. 10.2134/jeq2008.0201

Gburek, W. J., & Sharpley, A. N. (1998). Hydrologic controls on phosphorus loss from upland agricultural watersheds. *Journal of Environmental Quality, 27*(2), 267–277.

Gupta, H. V., Kling, H., Yilmaz, K. K., & Martinez, G. F. (2009). Decomposition of the mean squared error and NSE performance criteria: Implications for improving hydrological modelling. *Journal of Hydrology, 377*(1-2), 80–91.

Heathwaite, L., Sharpley, A., & Gburek, W. (2000). A Conceptual Approach for Integrating Phosphorus and Nitrogen Management at Watershed Scales. *Journal of Environmental Quality, 29*(1), 158–166. 10.2134/jeq2000.00472425002900010020x

Huang, J., Pedrera-Parrilla, A., Vanderlinden, K., Taguas, E. V., Gómez, J. A., & Triantafilis, J. (2017). Potential to map depth-specific soil organic matter content across an olive grove using quasi-2d and quasi-3d inversion of DUALEM-21 data. *Catena, 152*, 207–217. 10.1016/j.catena.2017.01.017

Kelley, J., Higgins, C. W., Pahlow, M., & Noller, J. (2017). Mapping Soil Texture by Electromagnetic Induction: A Case for Regional Data Coordination. *Soil Science Society of America Journal, 81*(4), 923–931. 10.2136/sssaj2016.12.0432

Khongnawang, T., Zare, E., Zhao, D., Srihabun, P., & Triantafilis, J. (2019). Three-dimensional mapping of clay and cation exchange capacity of sandy and infertile soil using EM38 and inversion software. *Sensors, 19*(18), 3936.

Kiflai, M. E., & Whitman, D. (2023). Geophysical mapping of freshwater lens in Big Pine Key, Florida: Electromagnetic Induction Calibration and Application. *Near Surface Geophysics, 21*(2), 152–167. 10.1002/nsg.12244

Kleinman, P. J. A., Church, C., Saporito, L. S., McGrath, J. M., Reiter, M. S., Allen, A. L., Tingle, S., Binford, G. D., Han, K., & Joern, B. C. (2015). Phosphorus Leaching from Agricultural Soils of the Delmarva Peninsula, USA. *Journal of Environmental Quality, 44*(2), 524–534. 10.2134/jeq2014.07.0301

Kleinman, P. J., Church, C., Saporito, L. S., McGrath, J. M., Reiter, M. S., Allen, A. L., Tingle, S., Binford, G. D., Han, K., & Joern, B. C. (2015). Phosphorus leaching from agricultural soils of the Delmarva Peninsula, USA. *Journal of Environmental Quality, 44*(2), 524–534.

Koestel, J., Kemna, A., Javaux, M., Binley, A., & Vereecken, H. (2008). Quantitative imaging of solute transport in an unsaturated and undisturbed soil monolith with 3-D ERT and TDR. *Water Resources Research, 44*(12)10.1029/2007WR006755

Krüger, J., Franko, U., Fank, J., Stelzl, E., Dietrich, P., Pohle, M., & Werban, U. (2013). Linking Geophysics and Soil Function Modeling—An Application Study for Biomass Production. *Vadose Zone Journal, 12*(4), vzj2013.01.0015. 10.2136/vzj2013.01.0015

Lavoué, F., Van Der Krak, J., Rings, J., André, F., Moghadas, D., Huisman, J. A., Lambot, S., Weiherrnüller, L., Vanderborght, J., & Vereecken, H. (2010). *Electromagnetic induction calibration using apparent electrical conductivity modelling based on electrical resistivity tomography*. Wiley. 10.3997/1873-0604.2010037

Lee, H., Ha, S., Hur, S., Jung, K., Kim, W., & Kim, K. (2006). Characteristics of soil water runoff and percolation in sloped land with different soil textures. *Korean Journal of Soil Science and Fertilizer, 39*(5), 268–273.

Martini, E., Werban, U., Zacharias, S., Pohle, M., Dietrich, P., & Wollschläger, U. (2017). Repeated electromagnetic induction measurements for mapping soil moisture at the field scale: Validation with data from a wireless soil moisture monitoring network. *Hydrology and Earth System Sciences, 21*(1), 495–513.

McLachlan, P., Blanchy, G., & Binley, A. (2021). EMagPy: Open-source standalone software for processing, forward modeling and inversion of electromagnetic induction data. *Computers & Geosciences, 146*, 104561. 10.1016/j.cageo.2020.104561

Mclachlan, P., Blanchy, G., Chambers, J., Sorensen, J., Uhlemann, S., Wilkinson, P., & Binley, A. (2021). *The Application of Electromagnetic Induction Methods to Reveal the Hydrogeological Structure of a Riparian Wetland*. American Geophysical Union (AGU). 10.1029/2020wr029221

McNeill, J. D. (1980). Electromagnetic terrain conductivity measurement at low induction numbers, Tech. *Note TN-6, 15*

Mester, A., Van Der Kruk, J., Zimmermann, E., & Vereecken, H. (2011). Quantitative Two-Layer Conductivity Inversion of Multi-Configuration Electromagnetic Induction Measurements. *Vadose Zone Journal, 10*(4), 1319. 10.2136/vzj2011.0035

Michael Mertens, F., Pätzold, S., & Welp, G. (2008). Spatial heterogeneity of soil properties and its mapping with apparent electrical conductivity. *Journal of Plant Nutrition and Soil Science, 171*(2), 146–154. 10.1002/jpln.200625130

Minsley, B. J., Kass, M. A., Hodges, G., & Smith, B. D. (2014). Multielevation calibration of frequency-domain electromagnetic data. *GEOPHYSICS, 79*(5), E201. 10.1190/geo2013-0320.1

Minsley, B. J., Smith, B. D., Hammack, R., Sams, J. I., & Veloski, G. (2012). Calibration and filtering strategies for frequency domain electromagnetic data. *Journal of Applied Geophysics, 80*, 56. 10.1016/j.jappgeo.2012.01.008

Moghadas, D., André, F., Bradford, J. H., van der Kruk, J., Vereecken, H., & Lambot, S. (2012). Electromagnetic induction antenna modelling using a linear system of complex antenna transfer functions. *Near Surface Geophysics, 10*(3), 237–247. 10.3997/1873-0604.2012002

Mwakanyamale, K., Slater, L., Binley, A., & Ntarlagiannis, D. (2012). Lithologic imaging using complex conductivity: Lessons learned from the Hanford 300 Area. *Geophysics, 77*(6), E397–E409. 10.1190/geo2011-0407.1

Needelman, B. A., Gburek, W. J., Petersen, G. W., Sharpley, A. N., & Kleinman, P. J. A. (2004). Surface Runoff along Two Agricultural Hillslopes with Contrasting Soils. *Soil Science Society of America Journal, 68*(3), 914–923. 10.2136/sssaj2004.9140

O'Leary, D., Brogi, C., Brown, C., Tuohy, P., & Daly, E. (2024). Linking electromagnetic induction data to soil properties at field scale aided by neural network clustering. *Frontiers in Soil Science, 4*10.3389/fsoil.2024.1346028

Robinson, J., Buda, A., Collick, A., Shober, A., Ntarlagiannis, D., Bryant, R., Folmar, G., Andres, S., & Slater, L. (2020). Electrical monitoring of saline tracers to reveal subsurface flow pathways in a flat ditch-drained field. *Journal of Hydrology, 586*, 124862. 10.1016/j.jhydrol.2020.124862

Selim, T., Amer, A., Farzamian, M., Bouksila, F., Elkiki, M., & Eltarabily, M. G. (2025). Prediction of temporal and spatial soil salinity distributions using electromagnetic conductivity imaging and regional calibration. *Irrigation Science,* , 1–19.

Sheets, K. R., & Hendrickx, J. M. (1995). Noninvasive soil water content measurement using electromagnetic induction. *Water Resources Research, 31*(10), 2401–2409.

Shober, A. L., Buda, A. R., Turner, K. C., Fiorellino, N. M., Andres, A. S., McGrath, J. M., & Sims, J. T. (2017). Assessing Coastal Plain Risk Indices for Subsurface Phosphorus Loss. *Journal of Environmental Quality, 46*(6), 1270–1286. 10.2134/jeq2017.03.0102

Soil Survey Staff. (2024). *Official Soil Series Descriptions.* https://casoilresource.lawr.ucdavis.edu/gmap/

Tan, X., Mester, A., Von Hebel, C., Zimmermann, E., Vereecken, H., Van Waasen, S., & Van Der Kruk, J. (2019). Simultaneous calibration and inversion algorithm for multiconfiguration electromagnetic induction data acquired at multiple elevations. *GEOPHYSICS, 84*(1), EN1. 10.1190/geo2018-0264.1

Thompson, J., Buda, A., Shober, A., Ntarlagiannis, D., Collick, A., Kennedy, C., Mosesso, L., Reiner, M., Triantafilis, J., Pokhrel, S., & Slater, L. (2025). Electrical geophysical monitoring of subsurface solute transport in low-relief agricultural landscapes in response to a simulated major rainfall event. *Journal of Hydrology, 646*, 132313. 10.1016/j.jhydrol.2024.132313

Vadas, P. A., Srinivasan, M. S., Kleinman, P. J., Schmidt, J. P., & Allen, A. L. (2007). Hydrology and groundwater nutrient concentrations in a ditch-drained agroecosystem. *Journal of Soil and Water Conservation, 62*(4), 178–188.

von Hebel, C., Rudolph, S., Mester, A., Huisman, J. A., Kumbhar, P., Vereecken, H., & van der Kruk, J. (2014). Three-dimensional imaging of subsurface structural patterns using quantitative large-scale multiconfiguration electromagnetic induction data. *Water Resources Research, 50*(3), 2732–2748. 10.1002/2013WR014864

Von Hebel, C., Rudolph, S., Mester, A., Huisman, J. A., Kumbhar, P., Vereecken, H., & Van Der Kruk, J. (2014). Three-dimensional imaging of subsurface structural patterns using quantitative large-scale multiconfiguration electromagnetic induction data. *Water Resources Research, 50*(3), 2732. 10.1002/2013wr014864

Von Hebel, C., Van Der Kruk, J., Huisman, J. A., Mester, A., Altdorff, D., Endres, A. L., Zimmermann, E., Garré, S., & Vereecken, H. (2019). *Calibration, Conversion, and Quantitative Multi-Layer Inversion of Multi-Coil Rigid-Boom Electromagnetic Induction Data*. MDPI AG. 10.3390/s19214753

Wait, J. (2012). *Geo-electromagnetism*. Elsevier.

Wang, C., & Slater, L. D. (2019). Extending accurate spectral induced polarization measurements into the kHz range: modelling and removal of errors from interactions between the parasitic capacitive coupling and the sample holder. *Geophysical Journal International, 218*(2), 895–912.

Zaru, N., Rossi, M., Vacca, G., & Vignoli, G. (2023). Spreading of Localized Information across an Entire 3D Electrical Resistivity Volume via Constrained EMI Inversion Based on a Realistic Prior Distribution. *Remote Sensing, 15*(16)10.3390/rs15163993

Zhang, G., & Feng, L. (2017). Recent progress and future prospect of digital soil mapping: A review. *Journal of Integrative Agriculture, 16*(12), 2871–2885.